Joshi, M., von Glasow, R., Smith, R. S., Paxton, C. G. M., Maycock, A. C., Lunt, D. J., Loptson, C. A., & Markwick, P. (2017). Global warming and ocean stratification: a potential result of large extraterrestrial impacts. *Geophysical Research Letters*, *44*(8), 3841-3848. https://doi.org/10.1002/2017GL073330

Global warming and ocean stratification: a potential result of large extraterrestrial impacts

Manoj Joshi[1,2], Roland von Glasow[1], Robin S. Smith[3], Charles G. M. Paxton[4], Amanda C. Maycock[5], Daniel J. Lunt[6], Claire Loptson[6], Paul Markwick[7]

[1] Climatic Research Unit, School of Environmental Sciences, University of East Anglia, Norwich, U.K.

[2] Centre for Ocean and Atmospheric Sciences, School of Environmental Sciences, University of East Anglia, Norwich, U.K.

[3] National Centre for Atmospheric Science, University of Reading, U.K.

[4] Centre for Research into Ecological and Environmental Modelling, University of St Andrews, St Andrews, U.K.

[5] School of Earth and Environment, University of Leeds, Leeds, U.K.

[6] School of Geographical Sciences, University of Bristol, Bristol, U.K.

[7] Getech PLC, Leeds, U.K.

Corresponding author: Manoj Joshi

Key Points:

- Large increases in stratospheric water vapor following large bolide impact events over the ocean cause positive radiative forcings
- Impact events are capable of warming climate and stratifying upper ocean over 1-2 decades even after initial surface cooling
- The process could have significantly reduced or possibly even reversed decadal cooling following Chicxulub impact

Abstract

The prevailing paradigm for the climatic effects of large asteroid or comet impacts is a reduction in sunlight and significant short-term cooling caused by atmospheric aerosol loading. Here we show, using global climate model experiments, that the large increases in stratospheric water vapor that can occur upon impact with the ocean, cause radiative forcings of over +20 Wm^{-2} in the case of 10-km sized bolides. The result of such a positive forcing is rapid climatic warming, increased upper-ocean stratification and potentially disruption of upper-ocean ecosystems. Since two thirds of the world's surface is ocean, we suggest that some bolide impacts may actually warm climate overall. For impacts producing both stratospheric water vapor and aerosol loading, radiative forcing by water vapor can reduce or even cancel out aerosol-induced cooling, potentially causing 1-2 decades of increased temperatures in both the upper ocean and on the land surface. Such a response, which depends on the ratio of aerosol to water vapor radiative forcing, is distinct from many previous scenarios for the climatic effects of large bolide impacts, which mostly account for cooling from aerosol loading. Finally, we discuss how water vapor forcing from bolide impacts may have contributed to two well known phenomena: extinction across the Cretaceous/Paleogene boundary, and the deglaciation of the Neoproterozoic snowball Earth.

1 Introduction

The effects of asteroid or comet impacts range from regional environmental devastation to potential contributions to mass extinctions [*Toon et al.,* 1997*, Alvarez et al.,* 2009*, Schulte et al.,* 2010]. It has usually been assumed that the climatic effect of a large impact over a few years is surface cooling, caused by large amounts of aerosols such as dust, soot and sulphate being lofted into the middle atmosphere, which lowers the amount of solar radiation reaching the surface [e.g. *Covey et al.,* 1994]. However, if an object impacts on the deep ocean, large amounts of water are released into the atmosphere [*Toon et al.,* 1997*, Pierazzo et al.,* 2010]; the resulting increase in stratospheric water vapor (henceforth SWV) can then act as an additional, significant radiative forcing agent.

Unlike aerosol, SWV does not sediment out of the stratosphere providing the environment remains sub-saturated, so its radiative effect on climate is likely to last longer than that of aerosol. Previous studies have concluded that approximately 10-300 parts per million (henceforth ppm), of SWV might remain in the stratosphere for several years following the impact of an extraterrestrial body, depending on its size [*Emiliani et al.,* 1981, *Toon et al.,* 1997*, Pierazzo et al.,* 2010]. Aerosol forcing is likely to be much smaller unless the bolide is large enough to strike the bottom of the ocean [*Covey et al.,* 1994, *Toon et al*., 1997]. The climatic effects of such a combined aerosol and stratospheric water vapor scenario are therefore important to quantify due to the high likelihood of a bolide striking the ocean as opposed to land.

To date, 3-D modelling studies have only examined the climatic effects of bolides of size 0.5-1 km, but the Chicxulub impact event at the end of the Maastrichtian is thought to have been caused by a bolide of approximate size 10 km [e.g. Schulte et al, 2010]. Furthermore, past modelling studies did not examine the response of the ocean or its circulation [*Pierazzo et al.,* 2010]. Quantification of the surface climatic response to SWV from impactors significantly larger than 1 km, having an order of magnitude more kinetic energy [*Toon et al.,* 1997], has been limited to inferences from idealized single-column models [*Toon et al.,* 1997].

Here, for the first time, we perform ensembles of 3-D coupled-ocean atmosphere model simulations and simplified energy-balance-type calculations to quantify multi-year effects of combined SWV and surface shortwave radiation perturbations resulting from hypothesized impact events larger than 1 km in size; we restrict our simulations to those regimes where the response is likely to be qualitatively different to cooling induced by virtual extinction of sunlight, noting that a very large reduction in surface shortwave radiation is inconsistent with evidence suggesting that photosynthesis and export productivity did not cease across the K-Pg bolide event [*Alegret et al.,* 2012], and certain organisms did not die out (see section 4), suggesting that low-latitude land regions did not completely freeze. Using the results from our semi-idealised modelling experiments, we discuss the potential application of our results to the Chicxulub impact event at the end of the Maastrichtian and their potential relevance in the context of deglaciation of the Neoproterozoic snowball Earth.

2 Methods

Two models are used in the analysis: FAMOUS ((FAst Met Office/UK Universities Simulator)- a coupled-ocean-atmosphere model, and a simpler energy balance model or EBM.

2.1 FAMOUS

FAMOUS is a coupled ocean-atmosphere global circulation model of horizontal resolution 7.5º x 5º (longitude x latitude) in the atmosphere and 3.75º x 2.5º in the ocean [*Smith et al.,* 2012a], and has been widely used in studies of climate and paleoclimate [e.g. *Smith et al.,* 2012b]. FAMOUS has near-identical physics and dynamics to the HadCM3 version of the Met Office Unified Model (MetUM) [*Gordon et al.,* 2000], which was used in the latest IPCC report, but is run at a lower spatial resolution. FAMOUS has the advantage of being computationally efficient, enabling the very long simulations required to spin up the ocean circulation for Maastrichtian boundary conditions, while retaining the complexity of a coupled-ocean atmosphere model utilizing the primitive equations of motion. Since it is not computationally feasible to run a full stratosphere-resolving chemistry-climate model on these timescales, and because we are primarily interested in the radiative rather than dynamical effects of stratospheric perturbations on the troposphere and surface, we focus on validating the radiative forcings (henceforth RF) and climate sensitivity simulated by FAMOUS against more complex models. Land average and global average surface air temperatures are 15.1±0.1°C and 23.0±0.1°C respectively in the "Maastrichtian" control run, and 8.0±0.1°C and 14.8±0.1°C in the "preindustrial" run- all of which are within 2°C of values obtained by other modelling work [*Hunter et al.,* 2013].

We apply the SWV RF by adding a globally constant water vapor perturbation to the atmosphere's radiative properties only (i.e. as seen by the model's radiation code) to all levels within the model's stratosphere, in a similar manner to previous work with versions of the MetUM [*Maycock et al.,* 2013]. The assumed SWV perturbations are shown in Table 1 and are 3 - 150 times ambient mixing ratios of 2-5 ppm, which is well within the range of SWV perturbations due to bolide impacts estimated in earlier studies [*Toon et al.*, 1997, *Emiliani et al.,* 1981]. The RF in the P, M, MD cases in Table 1 have been calculated using the method of *Gregory et al.* [2004]. The 3-6 year decay timescale of the SWV perturbation is chosen to be consistent with observations of age of air in the stratosphere [*Engel et al.,* 2009], and is shown in

Fig. S1(a). Offline RF calculations using the Edwards and Slingo radiative transfer code [*Maycock et al.*, 2011] incorporating a higher resolution representation of the stratosphere reveal differences in RFs between FAMOUS and the full radiative code of less than 10% (see S1). Water vapor in the troposphere in FAMOUS is transported and evolves self-consistently with the surface and hydrological cycle.

The effects of aerosol RF associated with a large impactor hitting the ocean bottom and lofting rocky ejecta into the atmosphere is approximated in the FAMOUS simulations by a reduction in the top-of-atmosphere solar forcing by 30%, equivalent to a top-of-atmosphere RF of -102 Wm^{-2}, which causes a surface shortwave RF whose maximum amplitude is -55 Wm^{-2}. Larger values of solar dimming of up to -80 Wm^{-2} are explored in the EBM. Aerosol sedimentation is parameterized by keeping the solar forcing perturbation constant for one year, followed by an exponential decrease in the perturbation over a timescale of one year, consistent with previous work [*Pierazzo et al.,* 2003], and is shown in Fig. S1(b). The maximum RF is lower than estimates from large impact events [*Pierazzo et al.,* 2003]. However, it should be noted that the RF value used in the present work is shortwave only: the forcing from aerosol particles greater than 1 μm in size is a residual of positive longwave and negative shortwave forcings that can each be much larger [e.g. *Timmreck et al.* 2010]. Recent work has suggested a range of short wave radiative forcing from soot aerosol from the Chicxulub impact of -100 to -200 Wm^{-2} [*Kaiho et al.,* 2016], implying a total surface radiative forcing that was lower in magnitude than this. Again, we note that a very large reduction in surface shortwave radiation is inconsistent with evidence suggesting that photosynthesis and export productivity did not cease across the K-Pg event [*Alegret et al.,* 2012], and certain organisms did not die out (see section 4), suggesting that low-latitude land regions did not completely freeze.

Each of the FAMOUS perturbation experiments is made up of 3 ensemble members which are each 50 years long, initialized from different points of the control run separated by 10 years in order to sample the effects of internal variability in the model. The model is run in two configurations: one representing the preindustrial Holocene Earth, and one representing the Maastrichtian stage 72.1-66.0 million years ago, in order to assess the sensitivity of our results to continental configuration (see Table 1). For more details of FAMOUS boundary conditions and configuration see Text S1.

2.2 Energy Balance Model (EBM)

The EBM resolves hemispheres and land-ocean contrasts, and represents heat exchange in the ocean using an upwelling-diffusion model [*Shine et al., 2005*]. The EBM assumes an equilibrium climate sensitivity parameter λ = 1.0 K $(Wm^{-2})^{-1}$, mixed layer depth = 75 m, and ocean diffusion $\kappa = 7.5 \times 10^{-5}$ $Km^{-2}s^{-1}$, so that the land and ocean temperature response in the absence of aerosol RF is similar to that of ensemble M3. The value of λ is consistent with the climate sensitivity of FAMOUS (see Text S1). The EBM is computationally very cheap and therefore ideal for investigating responses to many RF scenarios [*Shine et al.,* 2005*,* Appendix B]. Here, 336 EBM runs are performed with a combination of RF sources from SWV and solar dimming. The maximum SWV RF in the EBM is varied from +10 to +25 Wm^{-2}, corresponding to SWV perturbations of approximately 50 ppm to 300 ppm, and has the same time evolution as FAMOUS, shown in Fig. S1(a).

3 Results

We first examine the effects of SWV perturbations only (i.e. scenarios P1-P3 and M1-M3). A key measure of the environmental effects of any climatic forcing is the change in surface air temperature that it induces [*Collins et al.,* 2013]. Fig. 1 (a) shows area-averaged surface air temperature change over ocean (henceforth OSAT) and land (henceforth LSAT) in the two decades following the input of the SWV perturbations designed to mimic the possible effects of different sized bolide impacts into the deep ocean. The size of the response increases with SWV perturbation magnitude, with the largest perturbations of 300 ppm (in scenarios P3 and M3; see Table 1), exhibiting maximum OSAT increases of 5 K and 8 K respectively, and maximum LSAT increases of 9 K and 11 K respectively (see Fig. 1b), a few years after the impact.

The time at which the maximum temperature change occurs relative to the simulated impact increases in proportion with the temperature change, being 2-3 years for the smallest values (P1 and M1), to 5 years for the largest (P3 and M3). In general, LSAT changes show the same lag-time as OSAT changes, but are amplified by a factor of approximately 1.5. Without aerosol forcing, the rates of warming are more than an order of magnitude faster than the rate of global warming expected over the 21st century, and the warming patterns also display polar amplification (See Fig. S2), which is a well-known pattern of climatic change [*Collins et al*., 2013]. The differences between the responses for the present-day and Maastrichtian conditions is related to the albedo in each configuration. Run M0 has a lower planetary albedo than P0: 0.27 compared to 0.31, mostly due to lack of sea-ice in the warmer southern polar regions, which explains the former's higher globally averaged surface temperature. In addition, the maximum reduction in albedo following the input of the SWV perturbation is 12% in M3 compared to 3% in P3, suggesting a much stronger positive shortwave feedback in the Maastrichtian configuration, in addition to a stronger water vapor feedback due to higher concentrations of water vapor in the warmer atmosphere.

A key aspect of the warming signal is that it is not confined to the surface, but penetrates quickly into the upper ocean, increasing the static stability of this region, and inhibiting vertical motion. Such a response can restrict the transport of nutrients to the uppermost layers of the ocean [*Roemmich and MgGowan*, 1995, *Oerder et al.,* 2015], potentially disrupting surface oceanic ecosystems. Fig. 2 shows cross sections of the ocean temperature response averaged over years 1-10 after the SWV perturbation is imposed in a sample of the model ensembles: P2 (Fig. 2a), P3 (Fig. 2b), and M3 (Fig. 2c). In the tropics and subtropics, the warming response is confined mostly to the upper 100m of ocean. In the northern midlatitudes and southern subpolar regions, the warming signal penetrates downwards to 200-300m in depth. The scenarios with the largest increase in SWV display increases in upper ocean stratification whose consequences are to lower the magnitude of upwelling by up to 50% in upwelling regions (see Fig. S3), which are the regions where the majority of primary productivity occurs (e.g. Gregg et al. 2003). Key to this stratification is the rapid timescale of the warming (see Fig. 1).

As noted above the Chicxulub impact, which is thought to have contributed to the Cretaceous–Palaeogene extinction event (henceforth K-Pg event), approximately 66 million years ago [*Alvarez et al.,* 1980*, Schulte et al.,* 2010], likely caused significant injections of aerosols into the stratosphere by striking the ocean bottom [*Toon et al.,* 1997*, Covey et al.,* 2009]. We examine the combined effect of such a joint aerosol-SWV scenario in two ways:

firstly by introducing a parameterization of aerosol-induced surface cooling into the FAMOUS model (See Section 2.1); secondly by using the EBM, to quantify the sensitivity of OSAT and LSAT responses to uncertainties in SWV and surface shortwave radiative forcing.

LSAT and OSAT in the M2D and M3D "SWV plus solar dimming" FAMOUS experiments are shown by blue and red diamonds in Fig. 1 (a), and (b), respectively. Even with a change in surface shortwave radiation of -55 Wm^{-2}, ensemble M3D still exhibits a warming of up to 4 K (red diamonds), over 1-2 decades due to the warming effects of the SWV perturbation. Again, associated with the rapid warming is increased stratification of the ocean (see Fig. 2 (d)), which is not as large as that induced by SWV forcing alone (ensemble M3; Fig. 2 (c)), but does still cause a significant reduction in ocean upwelling (Fig. S4).

The climatic effects of a much larger range of SWV and surface shortwave radiative perturbations can be illustrated using the EBM. Fig. 3 shows land and ocean temperature responses in EBM runs that combine different magnitudes of cooling due to reduced surface shortwave radiation and warming due to increased SWV, with forcings in the four Maastrichtian climate model ensembles added for comparison. For certain combinations of forcings (e.g. a maximum negative surface RF = -40 Wm^{-2} and a maximum SWV RF = +24 Wm^{-2}) it is possible for the EBM to respond with a land temperature change is that is negative (regions with cold colours in Fig. 3 (a)), even though the largest upper ocean temperature change is positive (warm colours in Fig. 3 (b)), which implies an initial cooling of the land due to reduced sunlight, followed by warming of both land and ocean on a timescale of a decade or more.

4. Discussion and Conclusions

These results may shed new light on understanding changes in the environment and ecosystems around the K-Pg event. Terrestrial species are likely to have been adversely affected by immediate effects such as fires and a decrease in solar radiation [*Toon et al.,* 1997, *Schulte et al.,* 2010], and ocean productivity might be expected to be hindered by reduced sunlight in the first couple of years due to significant aerosol loading. However, accounting for the possible effects of SWV increases following a large impact to the ocean suggests possible longer term warming over land and enhanced ocean stratification, which may have adversely affected many oceanic and terrestrial species for at least a decade following the impact (see Fig. 2, Fig. S3 and Fig. S4).

Over land, crocodylomorphs (a group including crocodilians), chelonians (the order containing turtles), and champsosaurs with representatives in shallow marine and freshwater habitats seem to have survived better than other large bodied fauna [*Benton,* 1993, *MacLeod et al,* 1997, *Martin et al.,* 2014]. Large rivers might have been somewhat insulated from terrestrial temperature changes and fires, while estuarine areas might not have felt the full effects of marine stratification on nutrient supply: species living in such habitats might have therefore survived better than their fully oceanic or terrestrial counterparts, especially if they were tolerant to a wide range of different body temperatures.

The once in ~10^7-10^8 year occurrence of 10 km bolide impacts [Toon et al 1997] raises the possibility that such impacts could have played a role in the deglaciation of the Neoproterozoic snowball-Earth, given the ~5x10^7 yr timescale of the event. If the Earth's tropics

had been covered with ice and snow to any degree, the absence of weathering would cause CO_2 to build up in the atmosphere. However, even such CO_2 forcing is thought to have been too weak to deglaciate the tropical oceans if taken alone [e.g. *Le Hir et al.*, 2010]. In this situation, a bolide impact over a shallow sea would not only potentially provide a positive radiative forcing through darkening the tropical cryosphere by solid ejecta in a similar manner that has been postulated for the effects of dust (Abbot And Pierrehumbert 2010), but would also provide intense, if short-lived, SWV and cloud radiative forcings that might trigger deglaciation by amplifying the effect of the high background levels of CO_2. Future research should attempt to quantify both forcing and feedback effects further, given their sensitivity to the mean background state [*Pierrehumbert et al.* 2011].

Owing to the large uncertainties involved, we have not considered possible microphysical-chemical-climatic interactions following an impact event, such as: ozone depletion associated with large amounts of injected halogen-containing sea salt aerosol [*Pierazzo et al.,* 2010]; changes to SWV lifetime associated with increased oxidation of CH_4 by chlorine atoms; or HOx produced by large amounts of SWV. Large stratospheric aerosol loading might act to scavenge water, thus reducing SWV [*Pierazzo et al.,* 2010]. However, assuming a particle radius of 0.5 μm, a submicron aerosol source from the impact [*Toon et al.,* 1997] and an upper limit for a growth factor of sulphate aerosol of 5x (based on the growth of sulfuric acid particles under stratospheric conditions) we estimate that only a few percent of the SWV would be taken up by aerosol. Microphysical effects such as coagulation would also lower the magnitude of the RF from sulfate aerosol by increasing particle size [*Timmreck et al.,* 2010], as well as reducing aerosol residence time [*Pierazzo et al.,* 2003]. Additionally, a large stratospheric aerosol loading would warm the tropical tropopause, which might further increase SWV [*Joshi and Shine*, 2003]. Ice crystals might form, but even in the case with 300 ppm of SWV the stratosphere would only be supersaturated with respect to ice below about 20 km in altitude. Furthermore, there is a large uncertainty in the radiative effect of ice crystals because of factors such as ice crystal size and cloud optical depth [*Emiliani et al.,* 1981], which in turn depend on a variety of different processes, so the effects of ice crystals have not been considered here. The exact composition of aerosol (e.g. soot, dust, sulphate) would be expected to be different for different impact events. CO_2 increases resulting from impact events are extremely uncertain [*Royer,* 2014, *Huang et al.,* 2013], and have not been considered here.

We have explored potential climatic scenarios following extraterrestrial bolide impacts over the ocean that significantly raise stratospheric water vapor (SWV) levels. While short-term cooling and reduced primary productivity is likely to occur for impacts releasing aerosol into the atmosphere, the effects of increasing SWV may include rapid climate warming and increased ocean stratification on a timescale of 1-2 decades. The process could improve our understanding of periods such as the K-Pg extinction or the deglaciation of the Neoproterozoic snowball Earth, and indeed might reconcile differing viewpoints on the temporal and causal relationship between the Chicxulub impact and the K-Pg event itself [*Archibald et al.,* 2010, *Schulte et al,* 2010].

Acknowledgments

We acknowledge the support of resources provided by UK National Centre for Atmospheric Science (NCAS), the High Performance Computing Cluster supported by the Research and Specialist Computing Support service at the University of East Anglia, UK Natural Environment Research Council (NERC), grants "CPE" (NE/K014757/1), and "Paleopolar" (NE/I005722/1). . Data can be obtained from MJ on request. ACM acknowledges support from an AXA Postdoctoral Fellowship and the ERC ACCI grant Project No 267760, and NERC grant NE/M018199/1. We gratefully acknowledge the contribution of Roland Von Glasow, who played an integral role in the preparation of the original manuscript, but sadly passed away before its submission to Geophysical Research Letters. We also acknowledge useful input from K. Shine and J. Laube.

References

Abbot, D. S., and R. T. Pierrehumbert (2010), Mudball: Surface dust and snowball Earth deglaciation, J. Geophys. Res., 115, D03104, doi:10.1029/2009JD012007.

Alegret, L., E. Thomas, and K. C. Lohmann (2012), End-Cretaceous marine mass extinction not caused by productivity collapse, Proc. Natl. Acad. Sci. U.S.A., 109, 728-732.

Alvarez, L. W., W. Alvarez, F. Asaro, and H. V. Michel (1980), Extraterrestrial Cause for the Cretaceous-Tertiary Extinction, Science, 208, 1095-1108.

Archibald, J. D. et al. (2010), Cretaceous Extinctions: Multiple Causes, Science, 328, 973.

Benton, M. J. (1993), In The Fossil Record 2, Benton, M. J. Ed. (Chapman and Hall), pp 681-737.

Collins, M. et al. (2013), Long-term Climate Change: Projections, Commitments and Irreversibility. In: Climate Change 2013: The Physical Science Basis. Contribution of Working Group I to the Fifth Assessment Report of the Intergovernmental Panel on Climate Change [Stocker, T.F. et al. (eds.)]. Cambridge University Press, Cambridge, United Kingdom and New York, NY, USA.

Covey, C., S. L. Thompson, P. R. Weissman, and M. C. MacCracken (1994), Global climatic effects of atmospheric dust from an asteroid or comet impact on Earth, Global Planet. Change, 9, 263-273.

Emiliani, C, E. B. Kraus, and E. M. Shoemaker (1981), Sudden death at the end of the Mesozoic, Earth Planetary. Sci., 55, 317-334.

Engel, A. et al. (2009), Age of stratospheric air unchanged within uncertainties over the past 30 years, Nature Geosci., 2, 28-31.

Gordon, C. et al. (2000), The simulation of SST, sea ice extents and ocean heat transports in a version of the Hadley Centre coupled model without flux adjustments, Clim. Dynam., 16, 147-168.

Gregg, W. W., M. E. Conkright, P. Ginoux, J. E. O'Reilly, and N. W. Casey (2003) Ocean primary production and climate: Global decadal changes, Geophys. Res. Lett., 30, 1809, doi: 10.1029/2003GL016889

Gregory, J. M. et al. (2004), A new method for diagnosing radiative forcing and climate sensitivity, Geophys. Res. Lett., 31, L03205, doi:10.1029/2003GL018747.

Huang, C., G. J. Retallack, C. Wang, and Q. Huang (2013), Paleoatmospheric pCO_2 fluctuations across the Cretaceous–Tertiary boundary recorded from paleosol carbonates in NE China, Palaeogeogr. Palaeoclimatol. Palaeoecol., 385, 95-105.

Hunter, S. J., A. M. Haywood, P. J. Valdes, J. E. Francis, and M. J. Pound (2013), Modelling equable climates of the Late Cretaceous: Can new boundary conditions resolve data–model discrepancies? Palaeogeogr. Palaeoclimatol. Palaeoecol., 392, 41–51.

Kaiho, K., N. Oshima, K. Adachi, Y. Adachi, T. Mizukami, M. Fujibayashi, R. Saito (2016), Global climate change driven by soot at the K-Pg boundary as the cause of the mass extinction, Sci. Rep., 6, 28427, DOI: 10.1038/srep28427.

Le Hir., G., Y. Donnadieu, G. Krinner, and G. Ramstein (2010), Toward the snowball earth deglaciation…, Clim. Dynam., 35, 285-297.

Lunt, D. J. et al. (2016), Palaeogeographic controls on climate and proxy interpretation, Clim. Past, 12, 1181-1198, doi:10.5194/cp-12-1181-2016.

MacLeod, N. et al. (1997), The Cretaceous–Tertiary biotic transition, J. Geol. Soc., 154, 265–292.

Markwick, P. J., and P. J. Valdes (2004), Palaeo-digital elevation models for use as boundary conditions in coupled ocean-atmosphere GCM experiments: a Maastrichtian (late Cretaceous), example, Palaeogeogr., Palaeoclimatol., Palaeoecol., 213, 37-63.

Martin, J. E., R. Amiot, C. Lécuyer, and M. J. Benton (2014), Sea surface temperature contributes to marine crocodylomorph evolution, Nat. Commun., 5, 4658.

Maycock, A., K. Shine, and M. Joshi (2011), The temperature response to stratospheric water vapour changes, Quart. J. Royal Meteorol. Soc., 137, 1070-1082.

Maycock, A. C., M. M. Joshi, K. P. Shine, and A. A. Scaife (2013), The Circulation Response to Idealized Changes in Stratospheric Water Vapor, J. Climate, 26, 545-561.

Oerder, V., Colas, F., Echevin, V., Codron, F., Tam, J., and Belmadani, A. (2015), Peru-Chile upwelling dynamics under climate change, J. Geophys. Res., 120, 1152-1172.

Pierazzo, E., A. N. Hahmann, and L. C. Sloan (2003), Chicxulub and Climate: Radiative Perturbations of Impact-Produced S-Bearing Gases, Astrobiology, 1, 99-118.

Pierazzo, E., et al. (2010), Ozone perturbation from medium-size asteroid impacts in the ocean, Earth Planetary. Sci., 299, 263-272.

Pierrehumbert, R. T., D. S. Abbot, A. Voigt, and D. Koll (2011), Climate of the Neoproterozoic, Ann. Rev. Earth. Planetary Sci., 39, 417-460.

Roemmich, D., and McGowan, J (1995) Climatic Warming and the Decline of Zooplankton in the California Current, Science, 267, 1324-1326.

366 Royer, D. L. (2014), Atmospheric CO_2 and O_2 during the Phanerozoic: tools, patterns, and
367 impacts in Treatise on Geochemistry (2nd Edition), (Elsevier), chap. 6, pp. 251-267.

368 Schulte, P. et al. (2010), The Chicxulub Asteroid Impact and Mass Extinction at the Cretaceous-
369 Paleogene Boundary, Science, 327, 1214-1218.

370 Shine, K. P., J. S. Fuglestvedt, K. Hailemariam, and N. Stuber (2005), Alternatives to the Global
371 Warming Potential for Comparing Climate Impacts of Emissions of Greenhouse Gases,
372 Climatic Change, 68, 281-302.

373 Smith, R. S. (2012a), The FAMOUS climate model (versions XFXWB and XFHCC): description
374 update to version XDBUA, Geosci. Model Dev., 5, 269–276.

375 Smith, R., S. and Gregory, J. M. (2012b), The last glacial cycle: transient simulations with an
376 AOGCM, Climate Dynamics, 38, 1545-1559.

377 Timmreck, C. et al. (2010), Aerosol size confines climate response to volcanic super-eruptions,
378 Geophys. Res. Lett. ,37, L24705, doi:10.1029/2010GL045464.

379 Toon, O. B., K. Zahnle, D. Morrison, and R. P. Turco, and C. Covey (1997), Environmental
380 perturbations caused by the impact of asteroids and comets, Rev. Geophys. 35, 41-78.

381
382

Figure Captions

Figure 1. **(a),** Evolution of area-averaged surface air temperatures over the ocean (K), with time after the impact event. The lines show differences between P1-P0 (black solid); M1-M0 (black dashed); P2-P0 (blue solid); M2-M0 (blue dashed); P3-P0 (red solid); M3-M0 (red dashed); M2D-M0 (blue diamonds); M3D-M0 (red diamonds). **(b),** as (a), but for the difference in area-averaged surface air temperature over land (K). The thin dotted lines clarify 0 K changes.

Figure 2. (a), Latitude-depth cross section of the difference in zonally-averaged potential temperature (K), in the top 300m of the ocean between ensembles P2 (averaged in time between years 1 and 10 after the impact) and P0. Regions having values smaller than one interannual standard deviation in the control run are hatched in order to demonstrate the size of the signal compared to simulated natural variability. **(b),** as (a), but for difference between ensembles P3 and P0. **(c),** as (a), but for difference between ensembles M3 and M0. **(d),** as (a), but for difference between ensembles M3D and M0. Note the nonlinear contour intervals in each panel.

Figure 3. (a), Minimum annually averaged temperature change over land (K), between years 0-10 after a simulated impact calculated using several hundred simulations of the EBM showing the combined effect of aerosol and SWV RF[8]. The abscissa shows the most negative aerosol RF (Wm^{-2}), and the ordinate shows the maximum value of SWV RF (Wm^{-2}), in each individual EBM run. **(b),** as (a), but for the maximum annually averaged ocean mixed layer temperature response (K). FAMOUS ensembles M2, M2D, M3 and M3D are marked in grey in positions corresponding to their initial radiative forcings for comparison.

Table Captions

Table 1. Description of ensembles, maximum SWV perturbation, RF using radiative model of *Maycock et al,* [2011], regressed RF in Preindustrial (P), Maastrichtian (M), and Maastrichtian + Dimming (MD), cases, approximate corresponding impactor diameter, energy and return period *[Toon et al.,* 1997*, Emiliani et al.,* 1981].

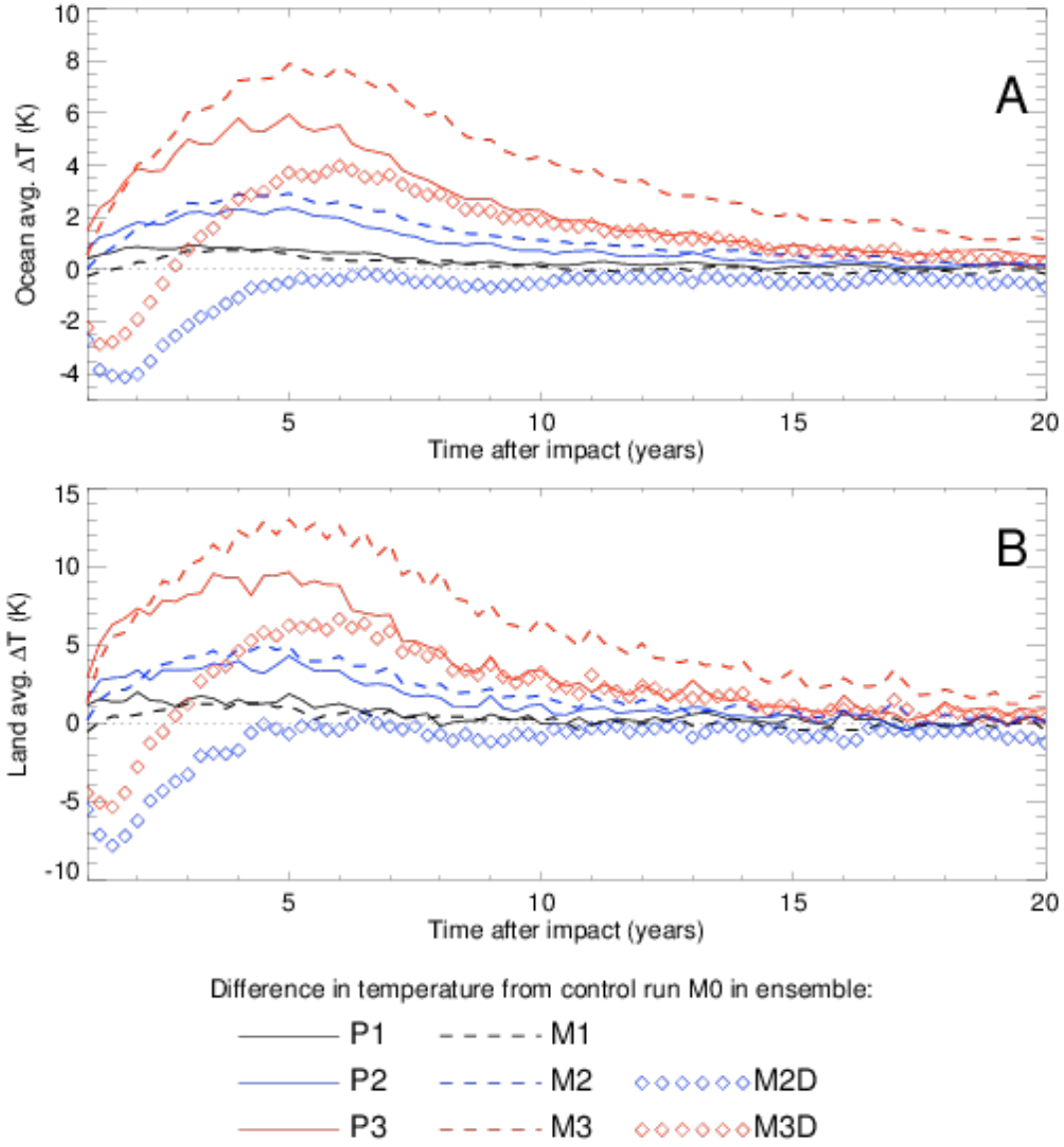

409

410 **Figure 1**. **(a),** Evolution of area-averaged surface air temperatures over the ocean (K), with time
411 after the impact event. The lines show differences between P1-P0 (black solid); M1-M0 (black
412 dashed); P2-P0 (blue solid); M2-M0 (blue dashed); P3-P0 (red solid); M3-M0 (red dashed);
413 M2D-M0 (blue diamonds); M3D-M0 (red diamonds). **(b),** as (a), but for the difference in area-
414 averaged surface air temperature over land (K). The thin dotted lines clarify 0 K changes.
415
416

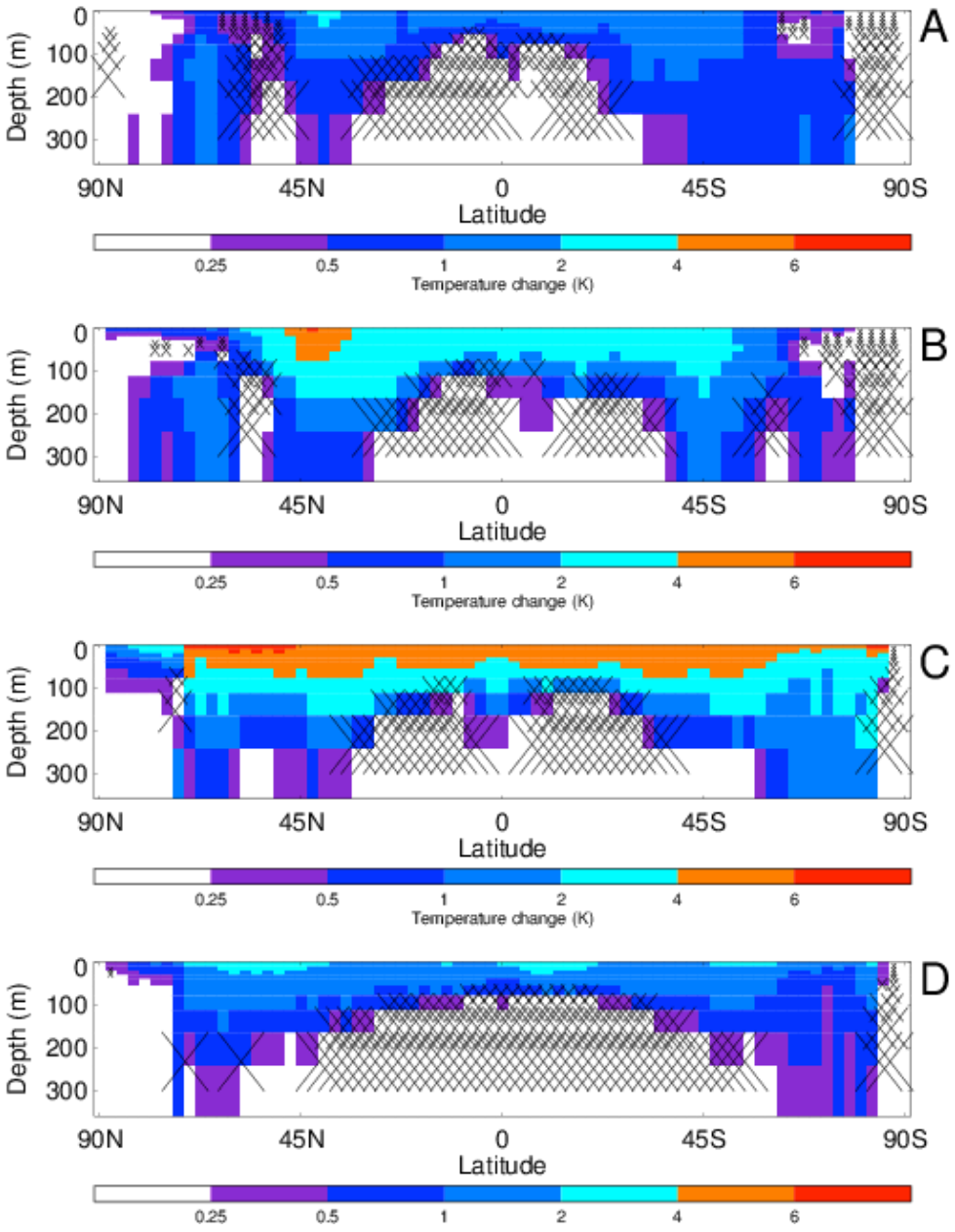

Figure 2. (a), Latitude-depth cross section of the difference in zonally-averaged potential temperature (K), in the top 300m of the ocean between ensembles P2 (averaged in time between years 1 and 10 after the impact) and P0. Regions having values smaller than one interannual standard deviation in the control run are hatched in order to demonstrate the size of the signal compared to simulated natural variability. **(b),** as (a), but for difference between ensembles P3 and P0. **(c),** as (a), but for difference between ensembles M3 and M0. **(d),** as (a), but for difference between ensembles M3D and M0. Note the nonlinear contour intervals in each panel.

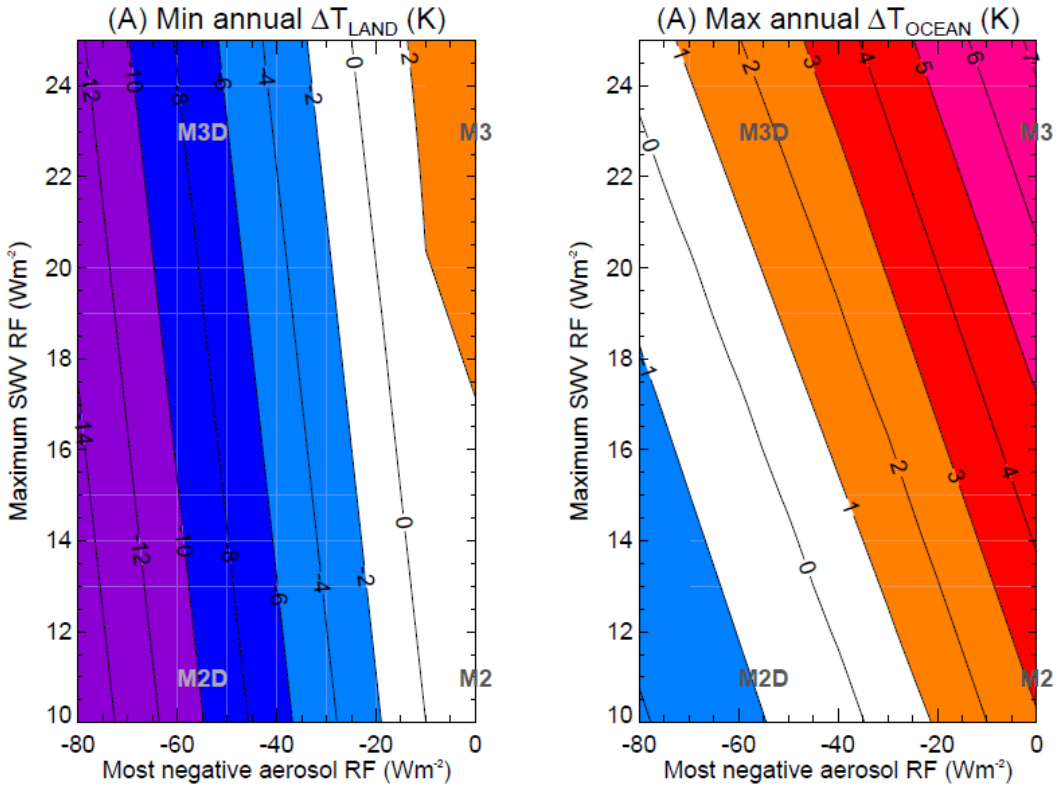

Figure 3. (a), Minimum annually averaged temperature change over land (K), between years 0-10 after a simulated impact calculated using several hundred simulations of the EBM showing the combined effect of aerosol and SWV RF[8]. The abscissa shows the most negative aerosol RF (Wm^{-2}), and the ordinate shows the maximum value of SWV RF (Wm^{-2}), in each individual EBM run. **(b),** as (a), but for the maximum annually averaged ocean mixed layer temperature response (K). FAMOUS ensembles M2, M2D, M3 and M3D are marked in grey in positions corresponding to their initial radiative forcings for comparison.

Impactor diameter (km)	-	~1	~3	~10
Impactor Energy (Mt)	-	10^4-10^5	~10^6	10^7-10^8
Impactor return period (years)	-	~10^5	~10^6	~10^7-10^8
SWV_{max} perturbation (ppm)	0	10	50	300
RF calculated using radiative model (Wm^{-2})	-	3.8	9.2	19.2
Preindustrial Runs	**P0**	**P1**	**P2**	**P3**
Maximum regressed preindustrial SWV RF (Wm^{-2})	-	3.4 ± 1.5	10.6 ± 2.0	22.0 ± 1.6
Maastrichtian Runs	**M0**	**M1**	**M2**	**M3**
Maximum regressed Maastrichtian SWV RF (Wm^{-2})	-	1.8 ± 1.4	11.1 ± 1.2	22.9 ± 0.8
Maastrichtian Runs with dimming	**M0**	-	**M2D**	**M3D**
Minimum value of surface solar dimming (Wm^{-2})			-55	-55

Table 1. Description of ensembles, maximum SWV perturbation, RF using radiative model of *Maycock et al,* [2011], regressed RF in Preindustrial (P), Maastrichtian (M), and Maastrichtian + Dimming (MD), cases, approximate corresponding impactor diameter, energy and return period *[Toon et al.,* 1997*, Emiliani et al.,* 1981].

Geophysical research Letters

Supporting Information for

Global warming and ocean stratification: a potential result of large extraterrestrial impacts

Manoj Joshi[1,2], Roland von Glasow[1], Robin Smith[3], Charles G. M. Paxton[4], Amanda C. Maycock[5,6], Daniel Lunt[7], Claire Loptson[7], Paul Markwick[8]

[1] Climatic Research Unit, School of Environmental Sciences, University of East Anglia, Norwich, U.K.

[2] Centre for Ocean and Atmospheric Sciences, School of Environmental Sciences, University of East Anglia, Norwich, U.K.

[3] National Centre for Atmospheric Science, University of Reading, U.K.

[4] Centre for Research into Ecological and Environmental Modelling, University of St Andrews, St Andrews, U.K.

[5] Centre for Atmospheric Science, Department of Chemistry, University of Cambridge, Cambridge, U.K.

[3] National Centre for Atmospheric Science, University of Cambridge, U.K.

[7] School of Geographical Sciences, University of Bristol, Bristol, U.K.

[8] Getech PLC, Leeds, U.K.

Contents of this file

Introduction

The supporting information consists of details of the two numerical models used, and four figures.

Text S1. Here we use version XFHCC of FAMOUS [*Smith et al.,* 2012], which applies a simple Rayleigh friction term over the top 3 levels of the atmosphere to parameterize the effects of breaking gravity or buoyancy waves that are poorly represented at this horizontal resolution. This significantly improves both the representation of the upper troposphere/lower stratosphere in FAMOUS and measures of troposphere variability. A simple parameterization specifies stratospheric ozone levels interactively based on whether they are below, at or above the tropopause, taking values derived from a modern climatology. The "pre-industrial" (denoted P) configuration (see Table 1) has greenhouse gases such as CO_2 and other boundary conditions such as continental distribution set to their values in 1850. The Maastrichtian configuration (denoted M) uses paleogeography (topography and bathymetry) created using similar techniques to previous work [*Hunter et al.*, 2013], based on published lithologic, tectonic and fossil studies, the lithologic databases of the Paleogeographic Atlas Project (University of Chicago), and deep sea (DSDP/ODP) data, underpinned by a globally integrated plate model based on structural geology, plate kinematics and geophysics [*Markwick and Valdes,* 2013]. The Maastrichtian runs use preindustrial levels of CO_2, which is on the lowest end of estimates of CO_2 during the end of the Cretaceous period [*Royer*, 2014], but still produce realistic amount of climatological Maastrichtian warming compared to the present day.

The pre-industrial control simulation for this version of FAMOUS was spun up for a thousand years, initialised from the pre-industrial climate of version XFXWB [*Smith et al.,* 2012] which had been run for more than 5000 years. The Maastrichtian spinup simulation was partly initialised from a HadCM3L simulation of the Maastrichtian time period which used the TRIFFID dynamic vegetation model [*Lunt et al.*, 2015]. The ocean state was used directly from the same HadCM3L simulation, which had been initialized as stationary with no initial flow, with an idealized zonally averaged temperature structure and salinity set to a constant 35 ppt, and run for 1400 years. Spatially-varying land surface properties (e.g. vegetation fraction and albedo) were derived from the HadCM3L simulation. The atmosphere was initialized from an arbitrary atmospheric state from a previous preindustrial simulation. FAMOUS was then spun up for 5000 years.

The RFs for the perturbed ensembles are shown in Table 1, and are calculated by plotting the simulated net flux at the top of the atmosphere against the globally averaged surface temperature difference between years 0-4 after the simulated impact and 10 different 4-year long segments of the relevant control run. The 4-year period is chosen as a balance between overestimation of RF from using too long a timescale when the RF is decreasing with time (see Figure 1), and very large uncertainties produced from using a shorter timescale. The plots are regressed to year 0 (i.e.: the time of impact), in a similar manner to previous methods [*Gregory et al.*, 2004], with the 95% confidence interval shown (see Table 1). The RF values in FAMOUS can be compared with results from a more complex radiative code with 15 levels in the stratosphere up to the 0.8 hPa level, which allows stratospheric temperatures to respond to the SWV perturbation, but does not allow any tropospheric change [*Maycock et al.,* 2011]. The RF values produced with the more complex code are approximately 10% smaller than the values produced by FAMOUS, showing that the SWV RF in FAMOUS is reasonable despite having only 2-3 levels in the stratosphere. The climate feedback parameter in FAMOUS is 1.10±0.05 $Wm^{-2}K^{-1}$, which is similar to HadCM3, being 1.32±0.08 $Wm^{-2}K^{-1}$, showing that the climate response of FAMOUS is consistent with other models used in global assessments of contemporary climate change [*Collins et al.,* 2013].

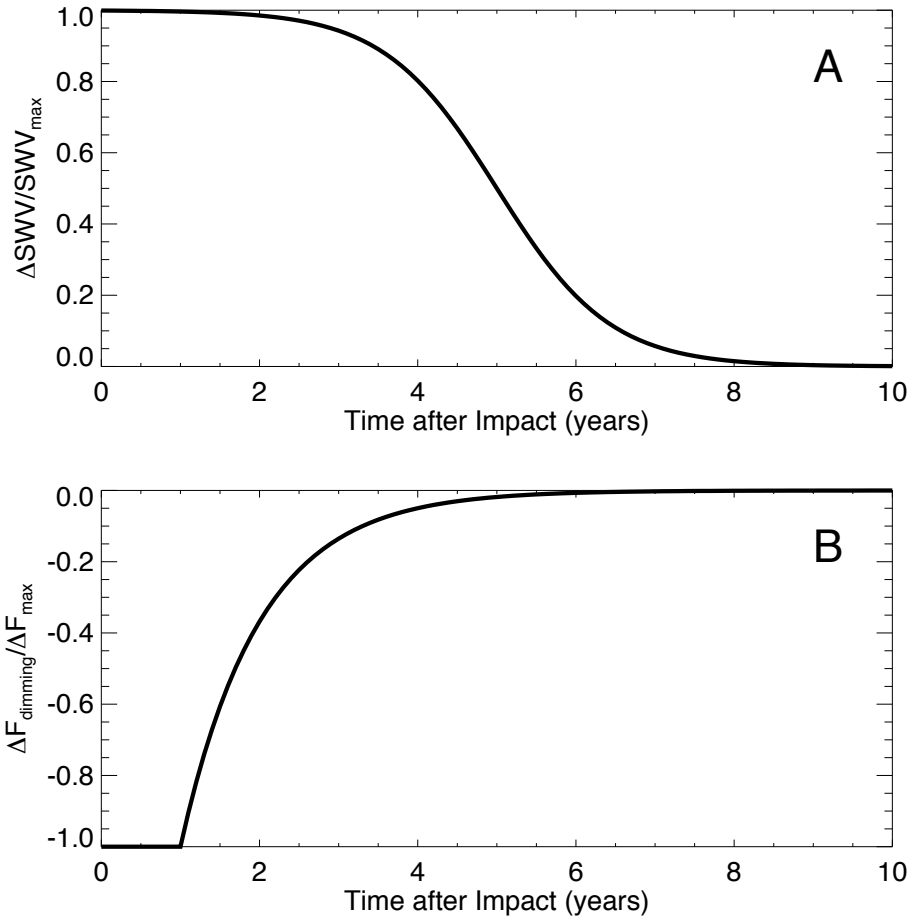

Figure S1. (a) Evolution of imposed SWV RF in FAMOUS normalized by SWV_{max}, whose values are given in Table 1 for each model ensemble. (b) Evolution of imposed solar dimming RF in FAMOUS normalized by its maximum amplitude, whose values are given in Table 1 for each model ensemble.

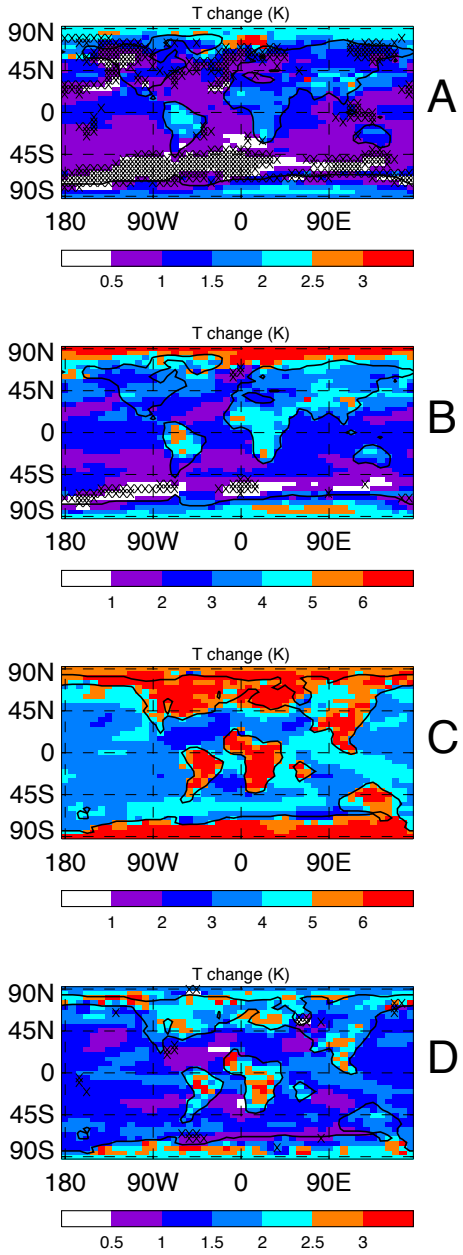

Figure S2. (a) Difference in surface air temperature (K) between ensembles P_2 and P_0 averaged in time between years 1.0 to 10.0 after the impact. Regions having values smaller than one interannual standard deviation in the control run P_0 are hatched. (b) as (a) but for difference between P_3 and P_0. (c) as (a) but for difference between M_3 and M_0. (d) as (a) but for difference between M_3D and M_0.

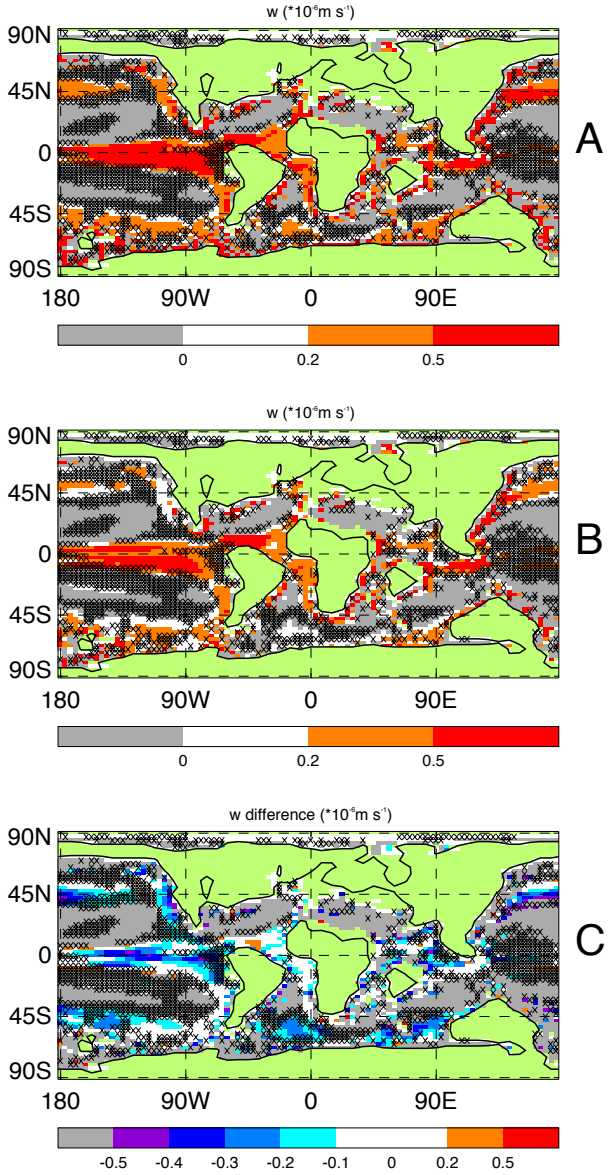

Figure S3. (a) Map of vertical velocity (10^{-6} ms^{-1}, upwards positive) at 96 m below the surface, i.e. below the mixed layer in the tropics and subtropics in run Mo. Areas with downwelling i.e. negative velocities have been greyed out for clarity. Regions having values smaller than one interannual standard deviation in the control run are hatched. (b) as (a) but for ensemble M3 in years 1-10 following the simulated impact. (c) Map of (b) minus (a); greyed out areas are as in (a), i.e. downwelling regions. In most upwelling zones vertical velocities have been reduced by up to 50%, which restricts nutrient supply to the topmost 100 m of the ocean.

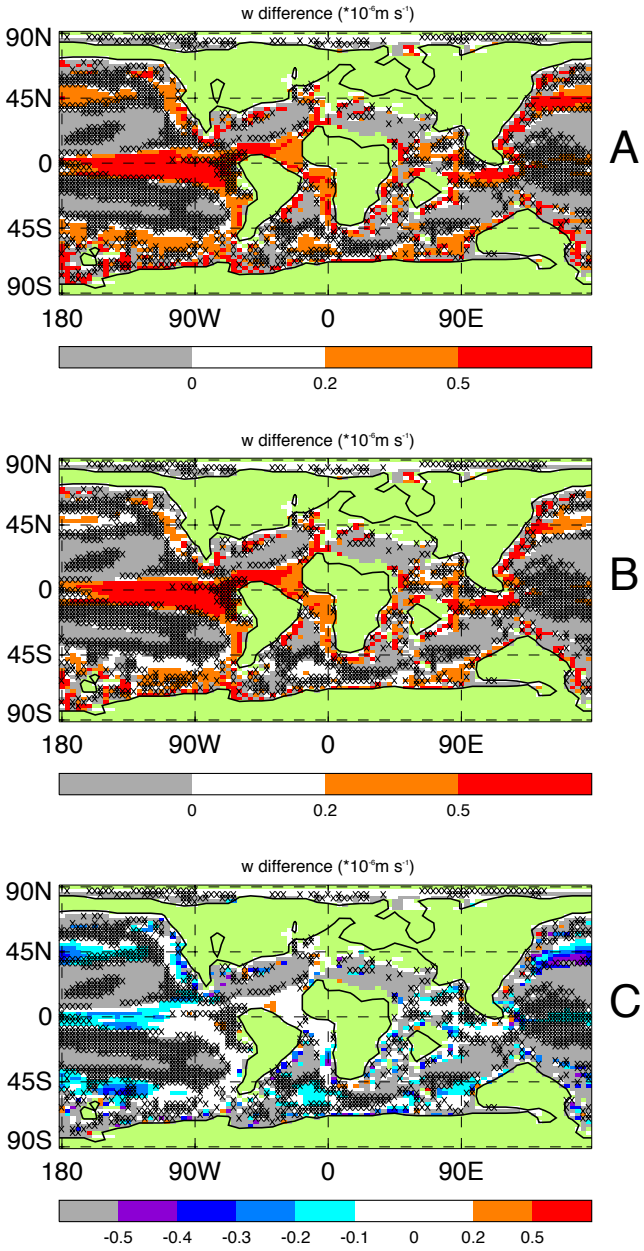

553

554 **Figure S4**. (a) as Fig. 3. (b), (c) as Fig. 3 but for ensemble M3D.

555

556